FIBER-OPTIC PRESSURE SENSOR FOR TIME-OF-FLIGHT MEASUREMENTS IN A SHOCK WAVE

by

KARTHIKEYAN JAGADEVAN

Presented to the Faculty of the Graduate School of
The University of Texas at Arlington in Partial Fulfillment
of the Requirements
for the Degree of

MASTER OF SCIENCE IN AEROSPACE ENGINEERING

THE UNIVERSITY OF TEXAS AT ARLINGTON

August 2010

To my mom, dad, sisters, friends and professors.

ACKNOWLEDGEMENTS

I would like to thank my research supervisor and professor, Dr. Frank Lu, for supporting me throughout my masters program, for being the driving force behind my work and allowing me to work at my pace, and for his understanding. I would also like to thank Dr. Haying Huang for providing useful suggestions and modifications that are required, I am grateful to her for allowing me to work in her lab to complete my initial testing of the experiments. I would also like to thank Dr. Nader Hozhabri for helping me with valuable information in order to proceed in the right direction to complete my graduate studies. I would also like to thank Dr. Donald Wilson and Dr. Wen Chan for their guidance as graduate advisors.

I would like to thank my friend Manjunath Shenoy for helping me at Dr. Haiying Huang's laboratory to set up the experiments and for helping me in operating them. I would like to thank my colleague Dr. Philip K. Panicker for supporting me during my graduate studies. He was always ready to help me. I would like to thank Prashaanth Ravindran for helping with LaTeX to write my thesis. I would also like to thank Adam Pierce, V. V. Suneel Jinnala, Hari Narayanan Nagarajan, Eric M. Braun and Richard R. Mitchell for their help and support during my research at the Aerodynamics Research Center. I would like to thank Alex Alphonse and Kermit Beird for helping in machining the parts. I would also like to thank Manda machines for helping me with the parts. I would also like to thank my friends Abhilash R. Menon, Jitesh Cherrukkadu Parambil, and Bharathkrishnan Muralidharan and Prajwal Shetty for their support and motivation that they provided during the stay at UTA.

I would like to thank all my friends and professors who made my life at UTA fruitful and fun. Nonetheless, I would like to thank my parents and sisters being with me during hard times and constantly encouraging me to reach new heights. I am always grateful to everyone who helped and supported me.

May 28, 2010

ABSTRACT

FIBER-OPTIC PRESSURE SENSOR FOR TIME-OF-FLIGHT MEASUREMENTS IN A SHOCK WAVE

Karthikeyan Jagadevan, M.S.

The University of Texas at Arlington, 2010

Supervising Professor: Frank K Lu

Fiber-optic sensors are widely employed to detect pressures and temperatures precisely. In particular, MEMS-based fiber-optic sensors are immune to electromagnetic interference but may have limitations at high temperatures as encountered in combustors. To ensure high-temperature survivability, such sensors may be bonded anodically. This project explains the development of a fiber-optic pressure sensor utilizing intensity based principle whereby a fused silica optical window was glued to the tungsten carbide enclosure. The development was estimated to determine high pressures of up to at least 3.5 MPa (507 psi). The sensor is designed to capture the pressure pulse and the time-of-flight (TOF) of a propagating detonation wave for implementation shock tubes.

Time-of-flight is critically important in detonation studies as it relates directly to the detonation wave velocity. Generally, the TOF is obtained by discrete sensors separated by a distance of at least a few cm. Thus, the propagation velocity, is strictly the average over that distance, thereby introducing a certain uncertainty. In order to obtain a point measurement, the separation distance between the sensors should be

kept as short as possible. Advances in MEMS and electro-optics have made it possible to devise such an integrated TOF sensor together with high-speed data acquisition.

TABLE OF CONTENTS

LIST OF FIGURES

LIST OF TABLES

CHAPTER 1

INTRODUCTION

1.1 Introduction

Time of flight (TOF) is an important parameter in the study of propagating shocks and detonation waves. For example, in a pulse detonation engine, TOF analysis shows that the wave accelerates during deflagaration-to-detonation before stabilizing at Chapman–Jouguet levels in the detonation tube [3]. Obtaining the TOF from two transducers spaced apart produces a certain level of uncertainty per [4, 5], which shows the importance of achieving a point measurement. What is needed is a device that can measure a propagating pressure disturbance from the propagating shock or wave at two consecutive points which are as close as possible. Though there are numerous pressure sensing devices that can be used in harsh environments [6, 7, 8, 9], a couple of miniature pressure sensors separated closely is required for the time-of-flight measurement. Advancements in MEMS technology [10, 11] and development in electronics facilitate the development of micro sensors with fast rise and fall time. In addition, a fast responding photodetector can be chosen in order to obtain the fast moving detonation wave velocity [12].

Optical fibers can also be considered in miniaturizing optical sensors. In this sensor design, an intensity based method is employed along with fiber optics to determine the deflection of a diaphragm which is related to the pressure of the wave. The optical principle is based on the Fabry–Perot interferometry principle [13] except that there are no interference patterns involved. Multi-mode fibers are used to receive the reflected light; hence the name modified Fabry–Perot method or inten-

sity based. Figure 1.1 shows a schematic of the operating principle of Fabry-Perot interferometry[14, 10]. The diaphragm deflects when an external load is applied on it. The variation of the height of the Fabry-Perot cavity below the diaphragm causes the intensity of the light incident on the optical fiber to change thereby producing the desired transduction result [10, 15, 16, 17, 18].

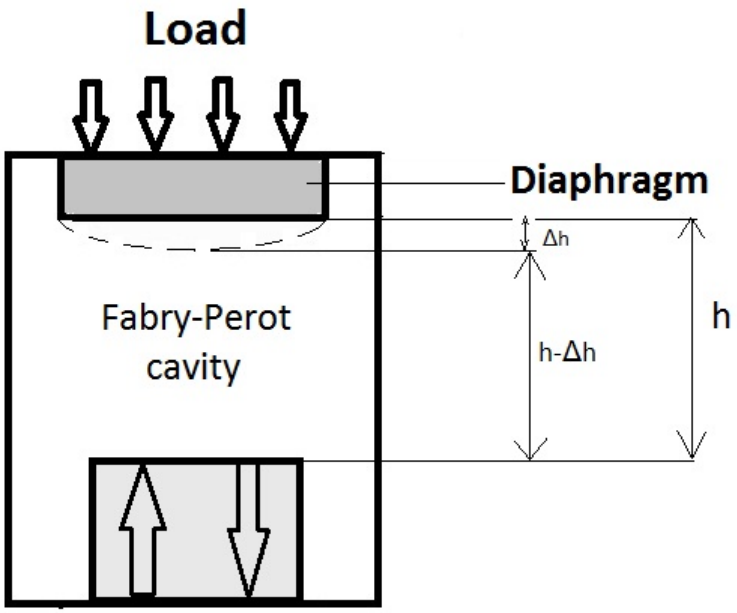

Figure 1.1. Fabry–Perot interferometry principle.

The design consists of a diaphragm, a cavity similar to that used in Fabry–Perot interferometry [19] and single and multi-mode fibers which are connected to the source and photodetector respectively. The pressure pulse from a detonation wave propagating past the sensor causes the diaphragm to deflect [7]. The intensity of the reflected light varies in the cavity due to the deflection of the diaphragm. This intensity variation is captured by the multi-mode fiber and recorded for further analysis.

In the intensity-based method, single mode and multi-mode fibers were used to send the incident light and receive the reflected light respectively. The deflections produced due to the pressure are related to the reflection of the light from the diaphragm to the the multi-mode fiber. Optical power received through the multi-mode fiber is converted to voltage in the photodetector and is observed in the oscilloscope.

We will discuss the design, development, calculations, calibration and testing, and results and recommendations of the transducer in further chapters.

CHAPTER 2

PRESSURE SENSOR DESIGN AND FABRICATION

Pressure is an important parameter to be measured in detonation studies. Various types of pressure transducers can be used for this purpose.

2.1 Time-of-Flight

According to [20], time-of-flight values and their uncertainty estimates are important parameters in characterizing propagating shock and detonation processes. In the classical time-of-flight method, the propagating disturbances pass through two sensors placed in series and the time of propagation can then be estimated. Though the TOF method seems to be simple, there is a certain level of uncertainity involved in it. Further, more sophisticated methods may be used to determine the propagation delay and to yield an uncertanity estimate.

In Figure 2.1 shown below, the first pressure spike was picked by the sensor 1 and the second was picked by the sensor 2 respectively. A time delay Δt arises as the pressure spike propagates from sensor 1 to sensor 2.

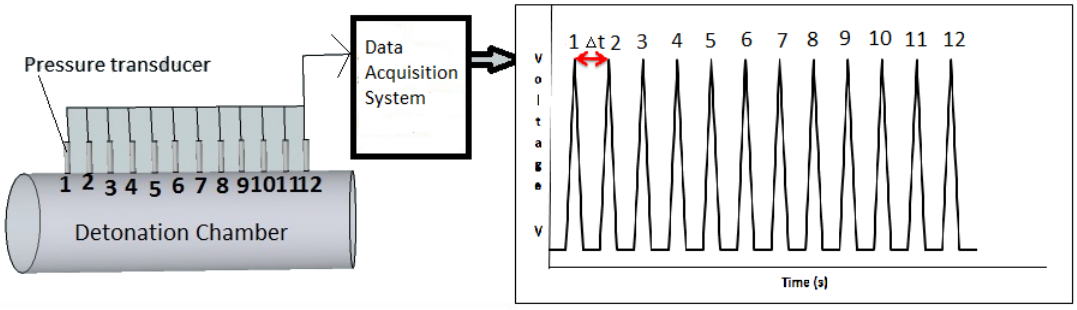

Figure 2.1. Time-of-flight concept.

The TOF $\tau \equiv \Delta t$ is obtained by placing the sensors 1 and 2 at a certain distance ζ, thus, propagation velocity,

$$u = \frac{\zeta}{\tau} \tag{2.1}$$

which is strictly the average over that distance, thereby introducing a certain uncertainty. The sensors should be kept as close as possible for a point measurement, hence reducing the level of uncertainty.

2.2 Conventional and Advanced MEMS Micromachining

Conventional micromachining follows the usual techniques of using the mechanical machining tools such as lathes, drills and other machining equipment. The proposed sensor design requires machinig of stainless steel and tungsten carbide tubes in order to assemble the parts as explained later in this chapter. The tungsten carbide tube needed a step to be machined in the top to allow a diaphragm to be properly seated. The electrical discharge machining technique [21] was used for this purpose, drilling a concentric hole through a tungsten carbide rod of length 70 mm and for creating a step of 1 mm diameter with a depth of 150 μm at the tip of the tungsten carbide.

Advanced MEMS techniques [22] like etching uses silicon wafers and other materials to fabricate the sensors, there were different methods and models implemented for fabrication. The size of the sensors can be miniaturized with the help these micro and nanofabrication technology.

Conventional microfabrication techniques were used to design the sensor instead of advanced MEMS techniques though the latter are more precise because the design was intended to be subsequently improved for temperature and flame front determination in the future. So a transparent diaphragm is required. Moreover, it

was determined that silicon nitride can be used as a substrate to glue a transparent optical window like glass, sapphire, diamond or cubic zirconia but was not possible because of the bonding properties of silicon nitride. So an optical window bonded to micro-sized tungsten carbide and stainless steel tubes with fiber optics was designed conventionally.

2.3 Design and Development

PCB pressure sensors [1], such as the model 111A24A, Figure 2.2, have been used to measure the pressure in the detonation experiments. However, these pressure transducers were placed at a certain distance from each other so that the propagation time is the average over that distance. In other words, the measurement is not a point measurement. A further, smaller source of error arises due to the large size of such sensors. A pressure sensor that is very small is required. Such a miniature sensor was designed so that two of them can be placed side-by-side in a housing with the same dimensions as a conventional pressure transducer housing. The diameter of a single PCB transducer is 5mm whereas the two micro pressure sensors were each 1.5 mm in diameter so that both of them can be housed in the 5 mm diameter housing of the PCB transducer. Electrical connections also can introduce small time delays due to the presence of stray capacitance. Thus, optical transmission using optical fibers was considered.

Another feature of the proposed design is its robustness and durability. Since it is protected by enclosures, it can withstand high temperatures and pressures. A water jacket [2] as shown in Figure 2.3 for which specifications are provided in the Appendix A that is available for PCB Model 111A24 [1] can be used.

Figure 2.4 shows that the sensor consisted of a diaphragm in tungsten carbide enclosures that were encased in an outer steel enclosure. This outer steel enclosure

Figure 2.2. Dynamic pressure sensor [1].

Figure 2.3. Water jacket [2].

was threaded to a water jacket (not shown). Different diaphragms were chosen in order to get the expected pressure results in the shock tube. The diaphragm was glued to the outer steel enclosure using high-temperature zirconia glue [23] and using 5-minute epoxy. The two steel tubes containing separately a single mode and a multi-mode optical fiber were encased in another larger steel tube. A cavity was formed by placing the tubes at a distance from the diaphragms. Two single-mode fibers were coupled to a 1×2 splitter [24] and were connected to the laser source using FC/PC connectors [24]. Similarly, the multi-mode fibers were connected to a 2×1 combiner [24] to a photodetector [12]. The light reflected from diaphragm traveled

in the multi-mode fibers and was sensed by the photodetector connected to a digital storage oscilloscope for further analysis.

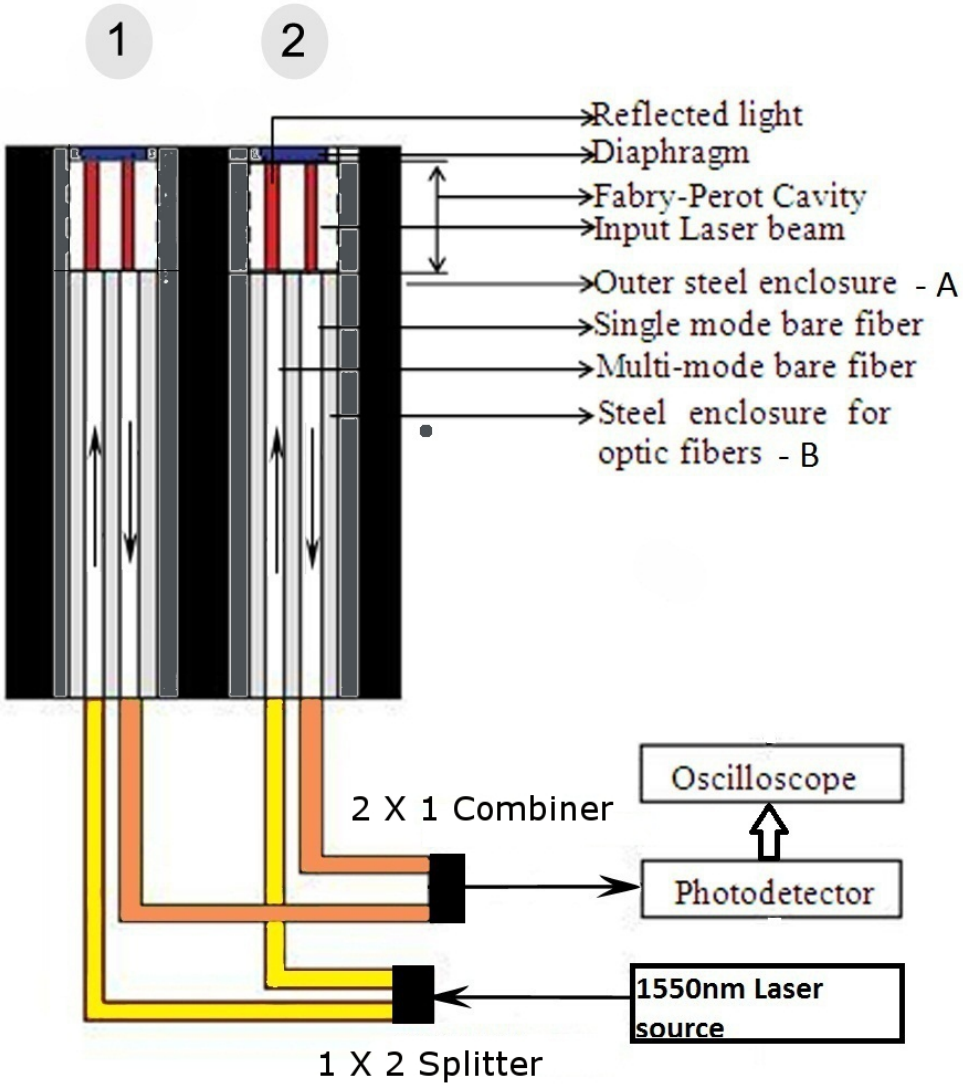

Figure 2.4. Schematic of FOPS.

The schematics were designed in Pro/E for the purpose of machining. Single mode and multi-mode bare fibers with 9/125 μm and 50/125 μm as core diameters respectively [25] were inserted in a hypodermic steel tube of dimensions 0.821 mm

O.D. and 0.250 mm I.D. Bare fibers are inserted in the hypodermic steel tubes and are glued using epoxy to avoid the breakage of fibers in the tube and to avoid irregularities in heights. The tips of the bare fibers are polished using various grits to attain maximum transmittance and receiving of light. Hypodermic steel tube is further inserted in another steel enclosure of O.D. 1.5 mm and I.D. 0.8211 mm. The diaphragm is finally glued on the steel enclosure which has 0.150 mm depth and 1 mm diameter on the top. The holes were drilled using wire EDM technology by Applegate [21]. 3D model of the complete assembly with two sensors and diaphragm designed in Pro/E is shown in Figure 2.5(b) and Figure 2.5(a).

2.4 Diaphragm

This transducer outputs pressure from mechanical deflections that occurs in the diaphragm due to the applied load [26]. The diaphragm was chosen according to temperature, rigidity, hardness and transparency for upgrading it to temperature measurement in future. Calculations with which the diaphragm was chosen are explained in the later chapter.

2.4.1 Types of Diaphragm Materials Examined

Since the sensor is designed to use at high temperatures and pressures, diamond was initially chosen because of the properties that it possesses. Considering cost as the factor, diamond was not used instead cubic zirconia was chosen since its properties were very similar to diamond.

Cubic zirconia (CZ) is mostly used in jewelry to replace diamonds. CZ material was sourced from India which was in diamond shape and it was machined using a grinder in the Material Science Engineering Department at University of Texas at Arlington and polished using a polisher. The surface was verified using SEM but

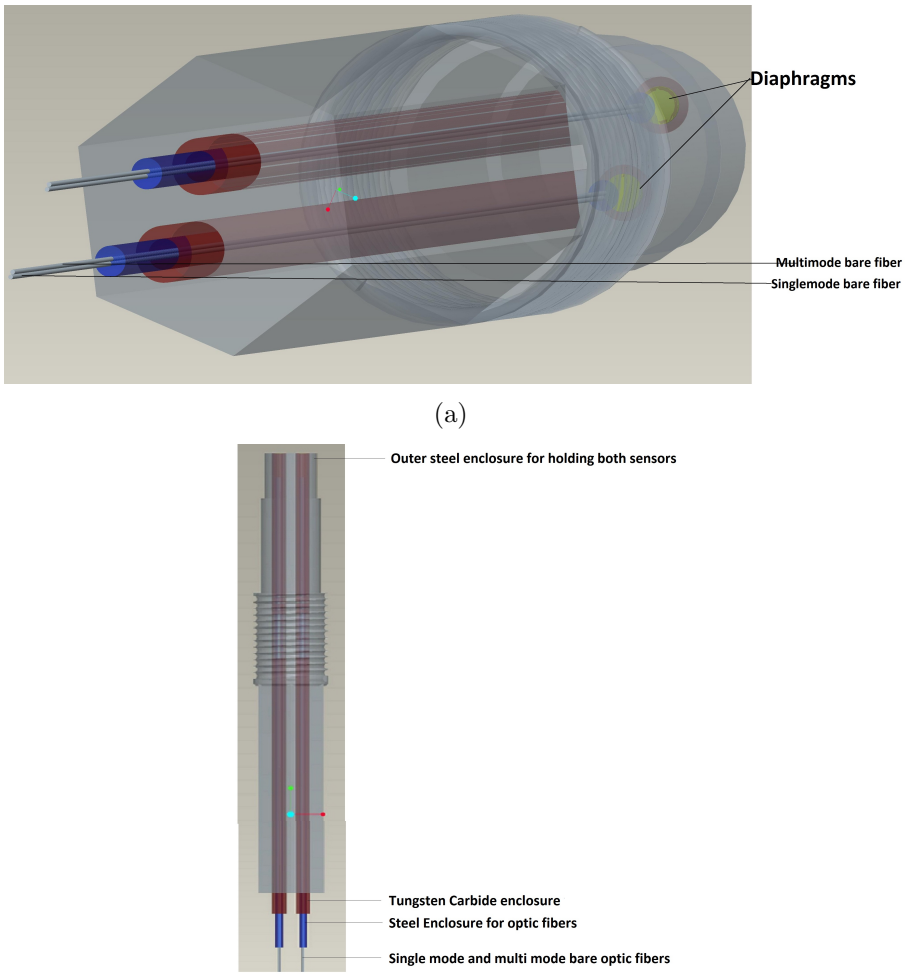

Figure 2.5. 3D model (a) Bottom view (b) Front view.

it was found that the hand machined cubic zirconia did not yield a sufficient a flat window. Since it was not possible to machine cubic zirconia manually with a 1 mm diameter and 150 μm thickness, cubic zirconia was not further considered as a diaphragm material.

The material that can withstand high temperatures next to cubic zirconia and which is transparent is fused silica. The fused silica flats from Tempotec [27] had a diameter of 1 mm and a thickness of 150 μm which made them suitable for the present

Table 2.1. Comparison between the properties of diamond and cubic zirconia

Properties	Diamond	Cubic Zirconia
Hardness	10,000 kg mm^{-2}	1300 kg mm^{-2}
Strength, tensile	>1.2 GPa	900 MPa
Strength, compressive	>110 GPa	-
Density	3520 kg m^{-3}	5680 kg m^{-3}
Young's modulus	1.22 GPa	200 GPa
Poisson's ratio	0.2	-
Thermal expansion coefficient	0.0000011 K^{-1}	10.3 10^{-6} K^{-1}
Thermal conductivity	20.0 W cm^{-1} K^{-1}	2 W cm^{-1} K^{-1}

purpose. The flat was glued to the outer steel enclosure using high-temperature zirconia glue. When compared to the dimensions of the diaphragm and the tungsten carbide tube, the cubic zirconia glue that was used was thicker when applied by hand and it covered the hole completely hence rendering the diaphragm useless. We needed a sophisticated device to apply the glue carefully along the circumference of the step provided at the top of the tube. Due to the constraint of funds, we were not able to use micro robotics to apply the glue. Also, the diaphragm was not deflecting and producing the expected results. The diaphragm may have been rigid along the corners due to excess glue or the diaphragm may have been thicker for such pressures and it did not deflect exactly as it was expected according to calculations.

Since the deflections were not satisfactory with cubic zirconia and fused silica between 0 and 600 psi, aluminum was next considered used as the diaphragm material with a thickness of 100 μm. Aluminum kitchen foil of that thickness was cut and glued using the 5-minute epoxy [28] and dried. Even after using aluminum, deflections were not as expected most likely due to applying the glue by hand.

2.5 Nano Fabrication

Conventional methods were not satisfactory, so advanced micro and nano fabrication were tried to solve the problem. As we know, these technologies are used to fabricate micro devices using silicon as the main ingredient. Though there are many nanofabrication techniques, most of them are for silicon and extending them to other materials is not an easy process.

The material in question is tungsten carbide [22, 29] which is conductive. Therefore, it appears that a diaphragm can be electroplated onto the sensing head but only if the hole through the center can be temporarily blocked by a filler. Existing facilities are not able to perform this operation either by electroplating or by using a microrobot to place a diaphragm or by growing a crystal diaphragm.

2.6 Fiber Optics

Optics were used due to low signal loss and fast response time. A single-mode bare fiber with 9/125 μm was used to send the laser light to be incident on the diaphragm. Multi-mode fiber with 50/125 μm was used to capture all the light that is reflected from the diaphragm. The fibers were kept as close together as possible to produce a compact design. The tips of the bare fibers were polished using various grits to attain maximum transmittance. The polishing procedure as provided by Thorlabs [30] was followed. Figure 2.6(a) shows the polished surfaces of the two sensors and Figure 2.6(b) shows the surface with single mode and multimode visble light through the optical fibers.

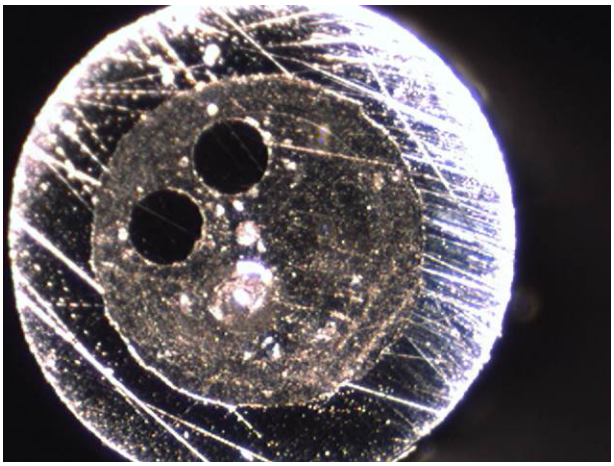

(a)

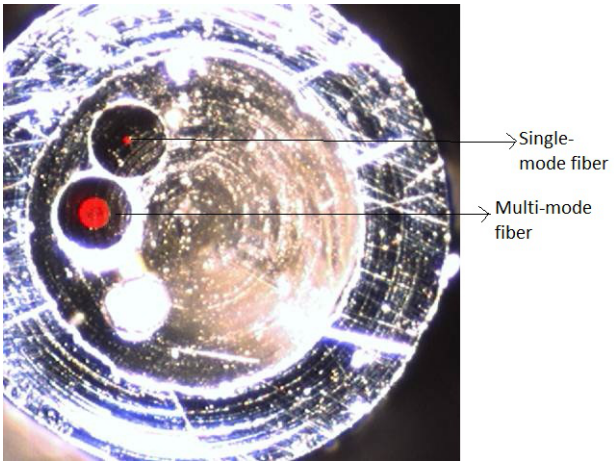

(b)

Figure 2.6. Polished bare fibers (a) Without light (b) With IR light.

CHAPTER 3

CALCULATIONS AND DERIVATIONS

3.1 Thin Plate Theory

According to [31], the following conditions are summarized from [32] for a true membrane:

1. The boundaries are free from transverse shear forces and moments. Loads applied to the boundaries must lie in planes tangent to the middle surface.
2. The normal displacements and rotations at the edges are unconstrained, that is, these edges can displace freely in the direction of the normal to the middle surface.
3. A membrane must have a smoothly varying, continuous surface.
4. The components of the surface and edge loads must also be smooth and continuous functions of the coordinates.

It was further shown that there are two more characterizations arrived from the above basic assumptions and they are:

1. Membranes do not have any flexural rigidity and therefore cannot resist any bending loads.
2. Membranes can only sustain tensile loads. Their inability to sustain compressive loads leads to wrinkling.

The von Kármán large deflection equations for thin plates were given as

$$\frac{\partial^4\Phi}{\partial x^4} + 2\frac{\partial^4\Phi}{\partial x^2\partial y^2} + \frac{\partial^4\Phi}{\partial y^4} = Eh\left[\left(\frac{\partial^2 w}{\partial x\partial y}\right)^2 - \frac{\partial^2 w\partial^2 w}{\partial x^2\partial y^2}\right] \tag{3.1}$$

$$\frac{\partial^4 w}{\partial x^4} + 2\frac{\partial^4 w}{\partial x^2\partial y^2} + \frac{\partial^4 w}{\partial y^4} = \frac{1}{D}\left(p + \frac{\partial^2\Phi\partial^2 w}{\partial y^2\partial x^2} + \frac{\partial^2\Phi\partial^2 w}{\partial x^2\partial y^2} - 2\frac{\partial^2\Phi}{\partial x\partial y}\frac{\partial^2 w}{\partial x\partial y}\right) \tag{3.2}$$

where $w(x,\, y)$ is the deflection of the plate, Φ is the stress function, E is Youngs modulus, h is the plate thickness, p is an applied pressure and D is the flexural rigidity. Further, thin plate theory with large deflections in a membrane can be found in [32]. In this sensor design, the focus is on thin clamped circular plate.

Moreover, [26] gives an analytical solution for a clamped circular diaphragm for large deflections. However, numerical techniques such as finite element analysis, boundary element analysis and finite difference amalysis can be used to predict the large deflections. Thin plate theory has to be used in the present case since the deflections are less than 1/5 of the diaphragm thickness [32, 33]. Since our design deflections is in the order of microns for a 1 mm diameter plate, thin plate or small deflection theory should be applied.

In order to design a diaphragm, strain, stress, and central deflections are to be considered and the governing equations are shown next [34, 35]. The radial and tangential strains at the center of the diaphragm are given by

$$E_{Rc} = E_{Tc} = \frac{3P_0^2(1-\nu^2)}{8t^2E} \tag{3.3}$$

where P = pressure (Pa), R_0 = diaphragm radius (mm), t = diaphragm thickness (mm) ν = Poisson's ratio and E = modulus of elasticity or Young's modulus (Pa) For a uniform applied pressure P, the radial deflection w_r of a glued diaphragm (clamped circular plate) [26, 33, 36, 37] is given as

$$w_r = w_c \left[1 - \left(\frac{r}{R_0}\right)^2\right]^2 \tag{3.4}$$

where r is the radial coordinate, R_0 is the radius of the diaphragm and D is the flexural rigidity, which is a measure of stiffness [26, 31, 33], given by

$$D = \frac{Et^3}{12(1-\nu^2)} \tag{3.5}$$

Also, [33, 34] give the following equation to calculate the maximum center deflection

$$w_c = \frac{PR_0^4(1-\nu^2)}{64D} = \frac{3PR_0^4(1-\nu^2)}{16t^3E} \tag{3.6}$$

Since the diaphragm is clamped, $r = 0$, and the central deflection of the diaphragm is given by

$$W = \frac{3PR_0^4(1-\nu^2)}{16t^3E} \tag{3.7}$$

and the sensitivity Y_c of the diaphragm is given by [38]

$$Y_c = \frac{3(1-\nu^2)}{16t^3E} \tag{3.8}$$

The sensitivity of the diaphragm can be increased by increasing the radius of the diaphragm and by decreasing the thickness [18].

3.2 Diaphragm Design Calculations

3.2.1 Manual Calculations

The thickness of the diaphragm has to be determined in order to design a diaphragm that gives a maximum deflection without being broken. The required thickness for the diaphragm was calculated from the above equations for various deflections. The appropriate thickness was obtained by substituting the properties of various materials in the above equations and by assuming the required deflections for different materials depending on the maximum reflection of light that will give the

Table 3.1. Calculated thickness from assumed deflection for cubic zirconia

Deflection (mm)	Thickness (μm)
0.002	123.0
0.005	90.6
0.01	71.9
0.015	62.8
0.020	57.1
0.025	53.0
0.03	49.9
0.035	47.4
0.04	45.3

peak value from the deflecting surface of the diaphragm. From (3.7) and (3.5) we get the equation to calculate the thickness,

$$t = \sqrt{\frac{0.75PR_0^2(1-\nu^{2)}}{e_0E}} \tag{3.9}$$

At a pressure of 6.9 MPa (1000 psi) and with assumed deflections, the thickness was calculated using (3.9) as shown in the tables below for different materials

3.2.1.1 Material I—Cubic Zirconia

Properties of cubic zirconia [39, 40]

Chemical formula: ZrO_2

Young's modulus or elastic modulus: 200 GPa Density: 5920 kg m^{-3}

Coefficient of thermal expansion: 8 $\times 10^{-6}$

Poisson's ratio: 0.28

Melting point: 2450 °C

Deflection of the diaphragm should be > 2 μm according to reflections received from the plain mirror used in the motor setup which is explained later in this chapter

Table 3.2. Diaphragm thickness and deflection for fused silica

Deflection (mm)	Thickness (μm)
0.002	175.2
0.005	129.1
0.01	102.4
0.015	89.5
0.020	81.3
0.025	75.5
0.03	71.0
0.035	67.5
0.04	64.5

and also [41] shows that the deflection should be at least one-third of the diaphragm thickness. Approximately 100 μm was chosen which is more than the calculated deflection as diaphragm thickness with a diameter of 1 mm so that there is a prominent deflection of the diaphragm without any fracture.

3.2.1.2 Material II—Fused Silica

Since machining of CZ was not precise, SiO_2 was also considered as a diaphragm material.

Properties of fused silica [39, 40]

Chemical formula: SiO_2

Young's modulus or elastic modulus: 73 GPa

Density: 2200 kg m^{-3}

Coefficient of thermal expansion: 0.55 $\times 10^{-6}$

Poisson's ratio: 0.17

Melting point: 1100 °C

Table 3.3. Diaphragm thickness and deflection forAluminum

Deflection (mm)	Thickness (μm)
0.002	171.4
0.005	126.3
0.01	100.2
0.015	87.6
0.020	79.6
0.025	73.9
0.03	69.5
0.035	66.0
0.04	63.1

A diaphragm thickness of 150 μm was chosen for a disk with diameter of 1 mm as thinner disks may be liable to crack.

3.2.1.3 Material III—Aluminum

Aluminum foil was chosen as a diaphragm material because fused silica was not deflecting since it is rigid when it is glued on the tungsten carbide enclosure.

Properties of aluminum [42]

Chemical formula: Al

Young's modulus or elastic modulus: 70 GPa

Density: 2702 kg m^{-3}

Coefficient of thermal expansion: 0.55 $\times 10^{-6}$

Poisson's ratio: 0.30

Melting point: 660 °C

From the data, a 1 mm diameter aluminum foil with a thickness of 80 μm is expected to give good deflections for the pressure range considered.

3.2.2 ANSYS Results

A three-dimensional model of the sensor was developed in ANSYS workbench, meshed and, for structural and thermal analyses were ran in it.

3.3 Fiber Optic Placement

The hypodermic steel tubes which house the single and multi-mode fibers were inserted in the tungsten carbide enclosure as discussed earlier and they were fixed at a particular distance where the multi-mode fibers received the maximum output from the reflecting diaphragm. The exact position was determined by using the motor setup available at the Advanced Sensor Technology Laboratory (ASTL) of the Mechanical and Aerospace Engineering Department. The graph in Figure 3.1 below shows a steady rise and fall of the points as the fiber tip moves with respect to the motor. The photodetector reads the values from the multi-mode fiber as the motor moves the fiber.[1]

After achieving the maximum intensity from the diaphragm, the fibers with the hypodermic tubing were placed at the position as shown in Figure 3.1 which is lesser than the peak reflecting point so that the diaphragm deflection will give a rise as the diaphragm deflection moves closer to the peak value.

[1]The data acquisition program was written by Dr. Haiying Huang.

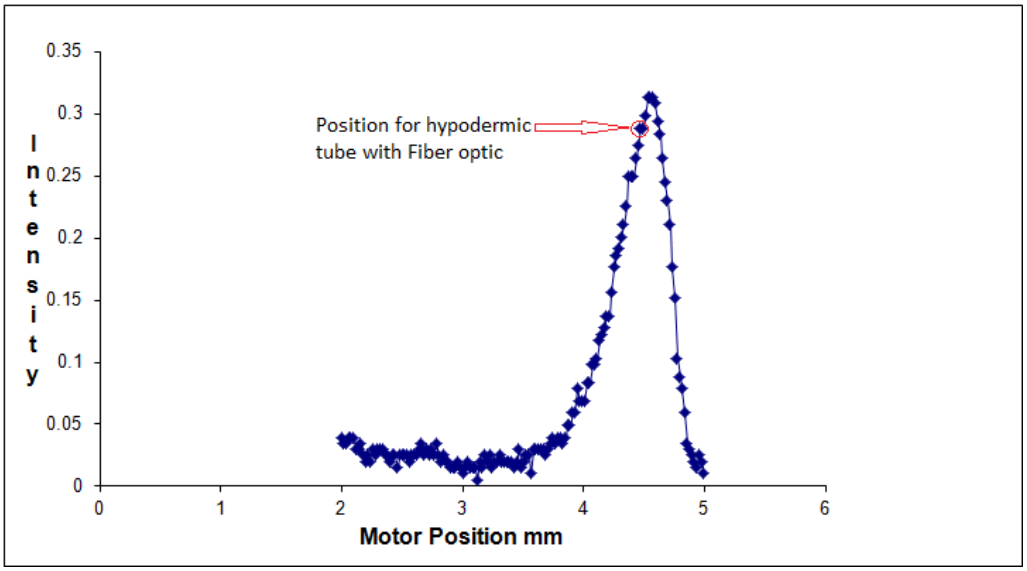

Figure 3.1. Motor position.

CHAPTER 4

RESULTS AND DISCUSSION

4.1 Calibration

Calibration plays an important role in deciding the various characteristics and parameters for any device.

4.1.1 Setup

The sensor has to be calibrated before being tested in the shock tube. Figure 4.1(a) and Figure 4.1(b) shows the calibration setup which consisted of a pressure bottle, an input pressure line, valves (V1 and V2), pressure gages (PG1 and PG2) and pressure regulator (Reg1). Since the pressure gauges (PG1 and PG2) were already calibrated, they were used as master gauges for pressure calibration. Input for the sensor was provided by a distributive feedback (DFB) bench-top laser source with a maximum optical power of 2 mW (see appendix B). The receiving end of the sensor was connected to a photodetector through a multi-mode fiber. The photodetector and a function generator (FG) were connected to the oscilloscope. An external amplifier and a high-pass filter were connected between the photodetector and the oscilloscope.

4.1.2 Operation

The diaphragm of the sensor deflects in accordance with the variations in pressure. A bottle of nitrogen at a pressure of 800 psi was connected to the input pressure line. A regulator was attached to the bottle to vary the pressure from 0 to 500 psi. The nitrogen from the bottle passed through valve (V1), pressure gage (PG1), pressure

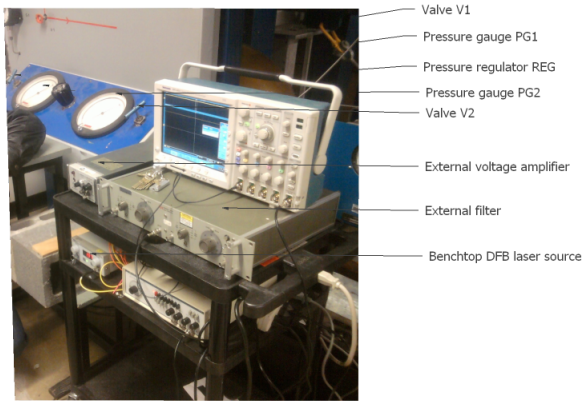

(a)

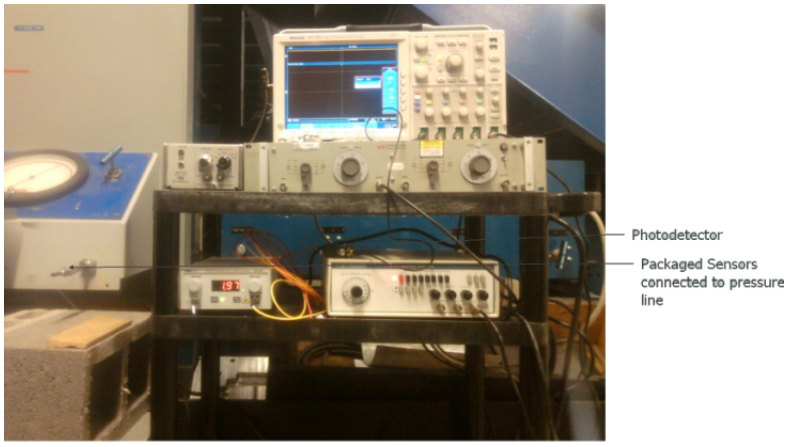

(b)

Figure 4.1. Calibration setup (a) View 1 (b) View 2.

regulator (REG), pressure gage (PG2) and valve (V2) respectively before reaching the diaphragm. Since the regulator in the bottle was not accurate, regulator (REG) was used. The changes in pressure were compared with both the regulators and matched. Also, the accuracy and preciseness of the reference devices (master gauges) played a major role in calibrating the pressure sensor.

The pressure was released from the bottle and the regulator which was connected to it was varied in steps of 50 psi. The valve (V1) was then opened, causing the regulated pressure from the bottle to pass through PG1 to REG. The pressure

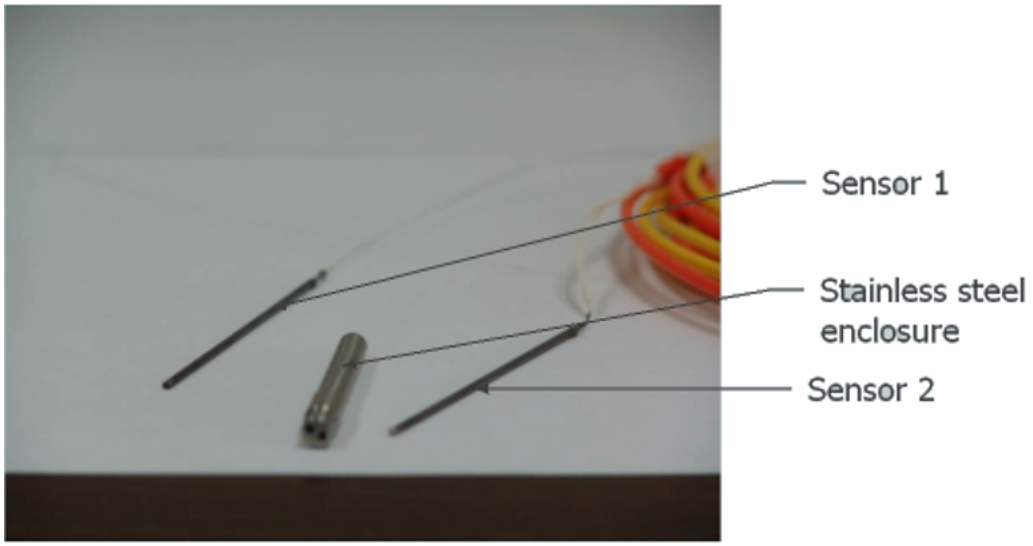

(a)

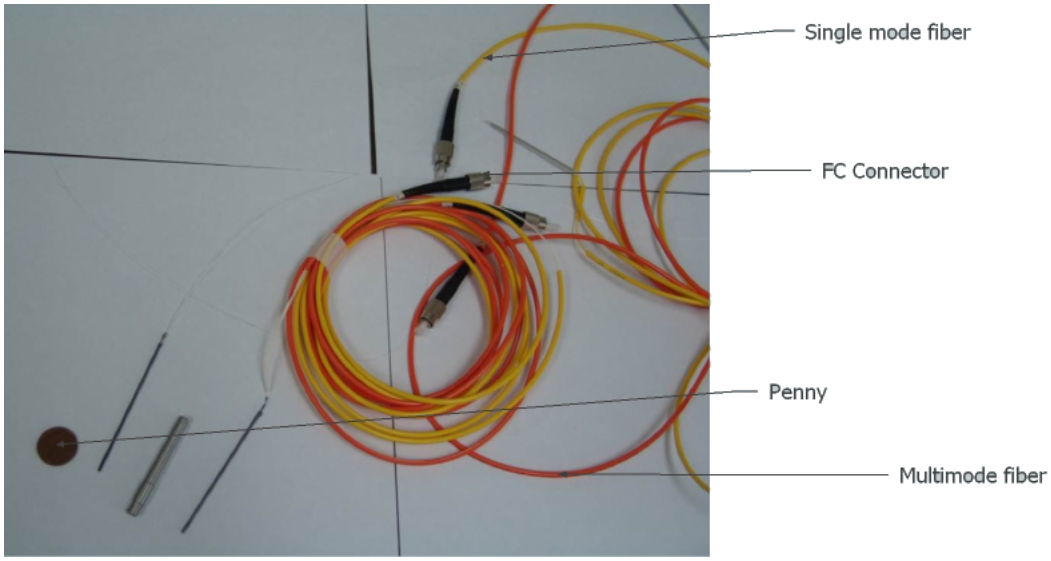

(b)

Figure 4.2. Unassembled sensors (a) Close view (b) Comparison with a penny.

regulator (REG) was adjusted in order to vary the pressure precisely. The pressure then flowed through PG2; valve V2 was opened and the sensor detected the pressure reading. Pressure readings in PG1 and PG2 were noted down respectively. The diaphragm consequently deflected according to the varying pressure noted in PG2. The

pressure transducer comprising two individual sensors were assembled in a stainless steel enclosure as shown in Figure 4.2(a) and Figure 4.2(b).

A single-mode fiber transmitted the input laser light to the bottom surface of the diaphragm and the multi-mode fiber received the reflections of the light from the diaphragm. The height variations in the Fabry–Perot cavity were converted to voltage using an integrated photodetector–amplifier. Output from the photodetector was sent to an external high-pass filter set at 60 Hz to remove lower frequency noise. The voltage from the photodetector was very small and had to be amplified with an external amplifier as shown in Figure 4.1(a). The oscilloscope received an input reference from the function generator (100 Hz frequency, 5 V_{pp}) and output from the photodetector. Filtered and amplified voltage readings were observed and saved using the oscilloscope.

4.1.3 Calibration Results and Discussion

Since the cubic zirconia wafers were hand machined, the required dimensions were not achieved. Thus, fused silica was used instead. Calibration set up was interfaced with LabVIEW [43] using BNC and coaxial cables. Though the cables were shielded, there was electronic noise which was removed using software filtering in LabVIEW. Pressure measurements were taken repeatedly at different conditions to test for consistency and repeatability. The pressure values used to calibrate the sensors ranged from 0 to 500 psi. The data acquired were plotted.

The set values in the LabVIEW were:

No of samples: 10000

Sampling rate: 200 Hz

High Pass filter: Stop frequency 65 Hz

Function Gen: 100 Hz

Acquisition time: 50 s

Applied pressure: 0 to 410 psi

Voltage amplification: $\times 100$

Figure 4.3(a) shows the plot between pressure and voltage. For a particular pressure reading, the voltage was averaged over time. A steadily increasing curve was observed with a voltage of 9.9 mV at 460 psi. In Figure 4.3(b), the voltage rose when there was an increase in pressure from 0 psi but the increase was slow. The maximum pressure threshold at which the sensor can operate was unknown and the maximum pressure delivered from the pressure bottle was only 460 psi. Though there was a steadily increasing curve, it was not linear. Similarly, Figure 4.3(c) shows that the voltage increased gradually. The external voltage amplifier had a phase shift which resulted in negative values of voltage.

The readings obtained from LabVIEW were as shown in Figure 4.4. For pressure values ranging from 0 to 500 psi, voltage readings were obtained using LabVIEW and plotted as shown in Figure 4.4(a). Figure 4.4(b) shows the interval from 0 to 0.5 s. At 0.01 s, a sharp spike was observed, implying the sensing of laser signals by the system though there were no deflections. The output in Figure 4.4(c) shows that from 0 to 0.5 s, the voltage had a steady value of approximately -0.675 V corresponding to 0 psi. When the pressure value increased, there was a shift in the voltage value to approximately -0.62 V. This trend continued till the 5 s mark, beyond which there were rapid fluctuations with increase in pressure. Figure 4.4(d) shows a close up view of the variations with pressures.

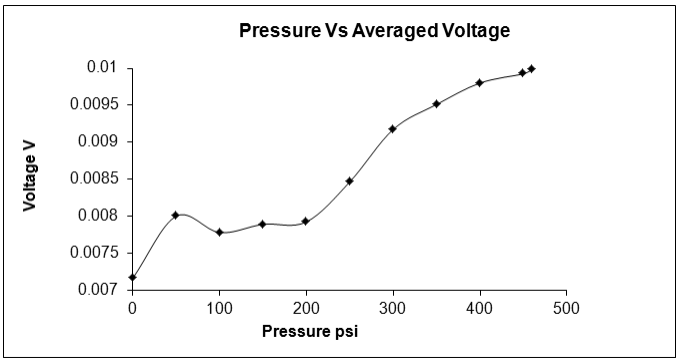

(a)

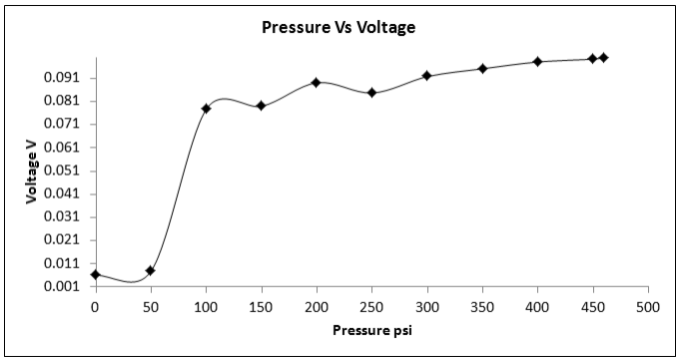

(b)

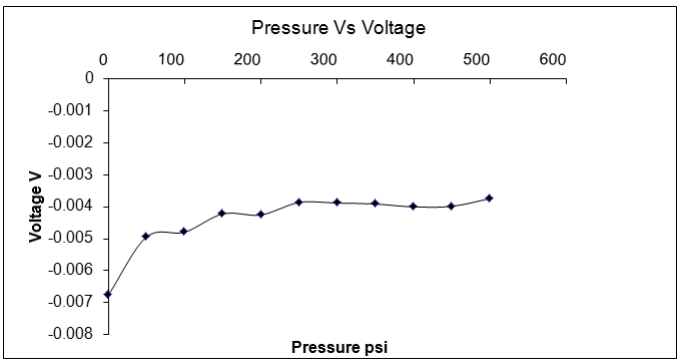

(c)

Figure 4.3. Pressure calibration tests Set 1 (a) Test 1(b) Test 2 (c) Test 3.

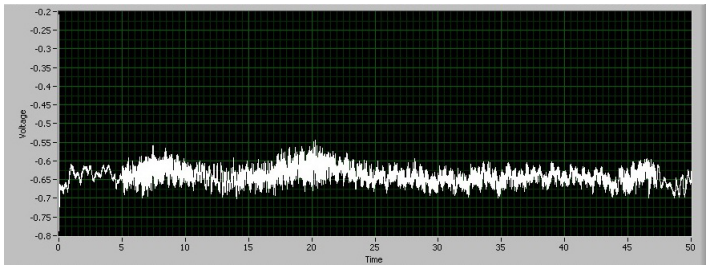

(a)

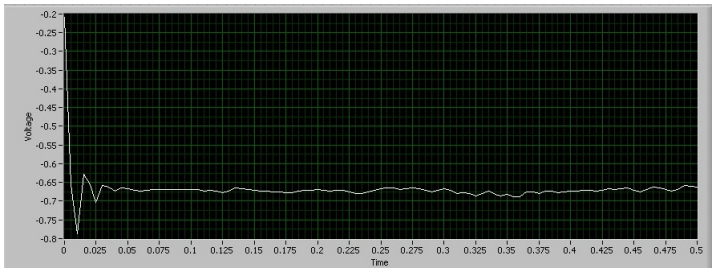

(b)

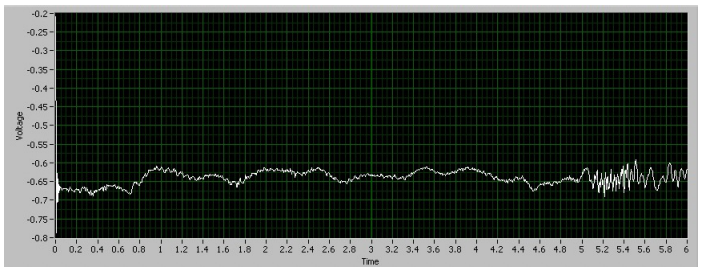

(c)

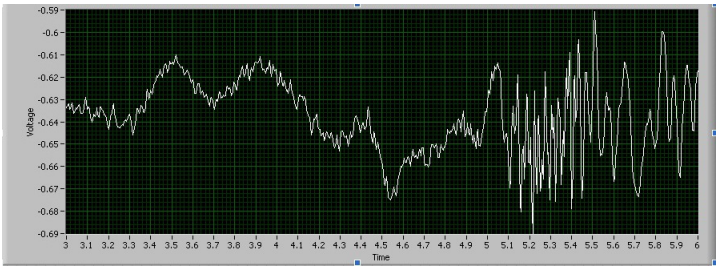

(d)

Figure 4.4. Voltage readings from Labview (a) 50 secs (b) 0.5 secs (c) 0 to 5 secs (d) Variations after 5 secs when pressure is applied.

No of samples per sec: 5000

High Pass filter: Stop frequency 60Hz

Function Gen: 100Hz

Time: 5secs

Applied pressure: 0 to 300psi

Voltage amplification: $\times 100$

Figure 4.5(a) shows a sharp rise in the voltage at 250 psi. A noticeable change in the plots around 200–250 psi was consistently observed, indicating a deflection in the diaphragms. There is a noticeable rise in the curve which is almost linear,as seen in Figure 4.5(b). Although, fluctuations are present, it rises to attain a steady state after 400 psi. However, the graphs were not consistent and everytime there were variations in the readings obtained.

Though there were prominent spikes in the voltage readings with respect to various pressure values, they were inconsistent. In the absence of concurring readings, the range of the sensor could not be decided and the exact pressure with respect to the voltage could not be determined. In order to check for repeatability, pressure cycling was carried out. Figure 4.6(a), Figure 4.6(b), Figure 4.6(c), Figure 4.6(d) and Figure 4.6(e) shows the same. Although the graphs show readings in the return path, precision was not observed. From the results it was observed that the variations were erratic and random.

Since the results were not satisfactory, it was thought that the diaphragms, which were glued to the tungsten carbide enclosures, may have been rigid along the circumference. This probably constrained their deflections. Another probability could

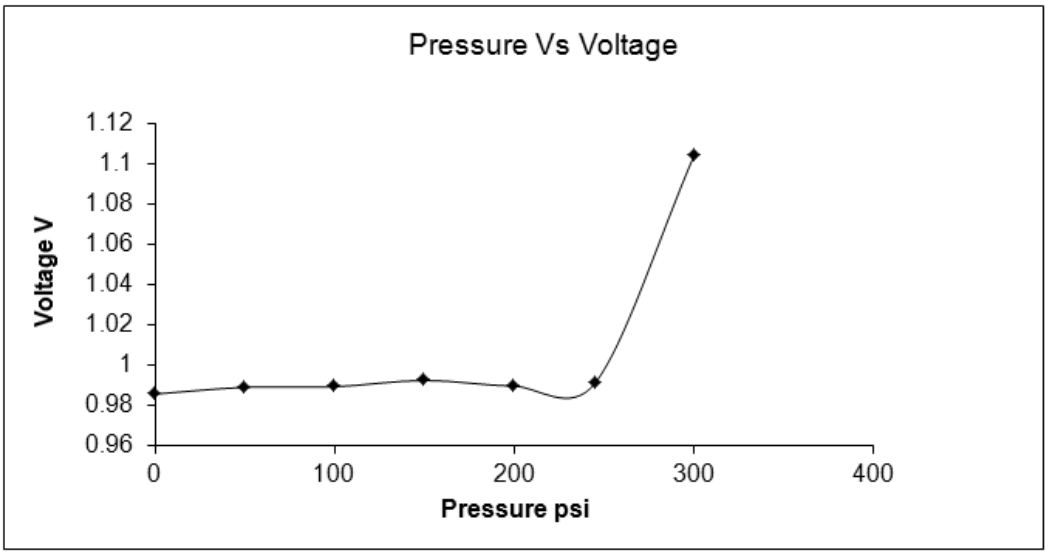

(a)

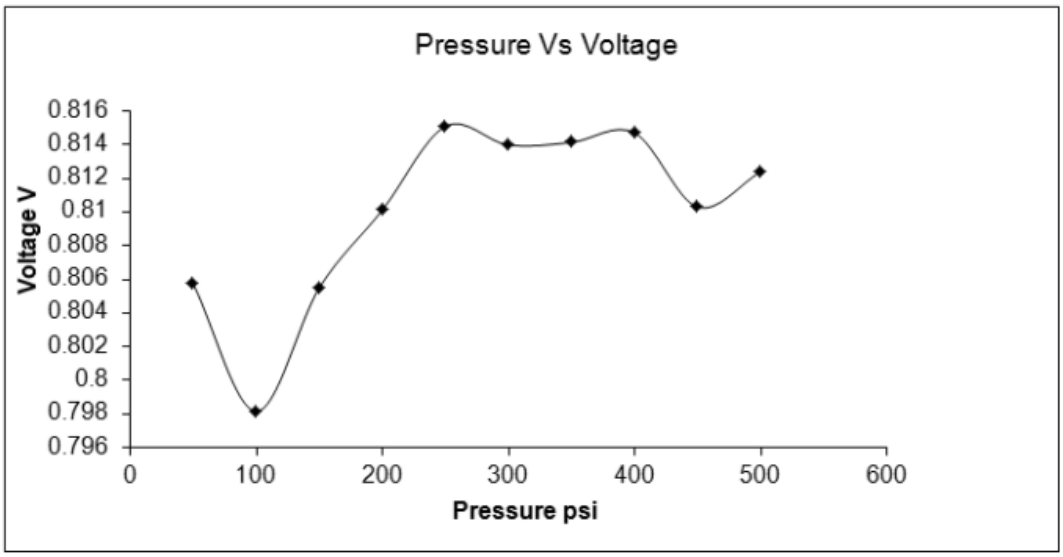

(b)

Figure 4.5. Pressure Calibration Tests Set 2 (a) Test 1 (b) Test 2.

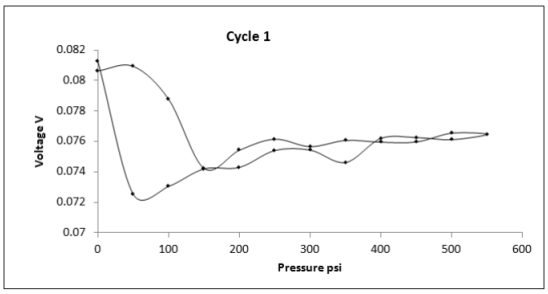

(a)

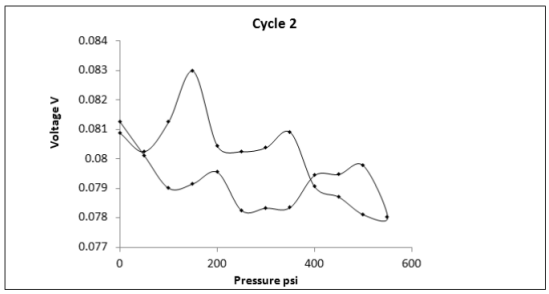

(b)

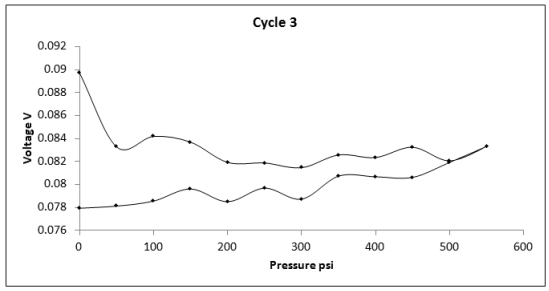

(c)

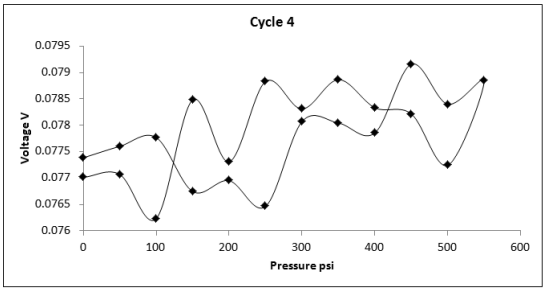

(d)

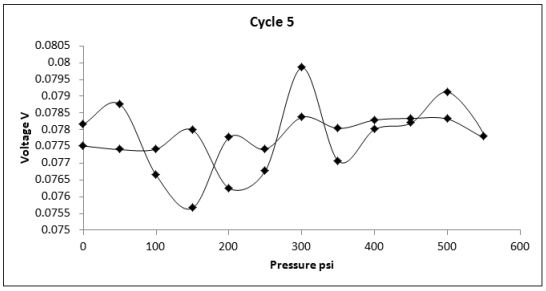

(e)

Figure 4.6. Pressure Calibration Tests Cycles (a) Cycle 1 (b) Cycle 2 (c) Cycle 3 (d) Cycle 4 (e) Cycle 5.

be that fused silica diaphragm used was thicker than required. Subsequently, a thin kitchen foil made of Aluminum with 1 mm diameter and 80 μm thickness was used as the diaphragm. The calibration tests were performed for a single run for pressure values ranging from 0–730 psi as well as pressure cycling from 0–600 psi.

Figure 4.7 shows the plot for an aluminum diaphragm but the readings observed were not linear and erratic.

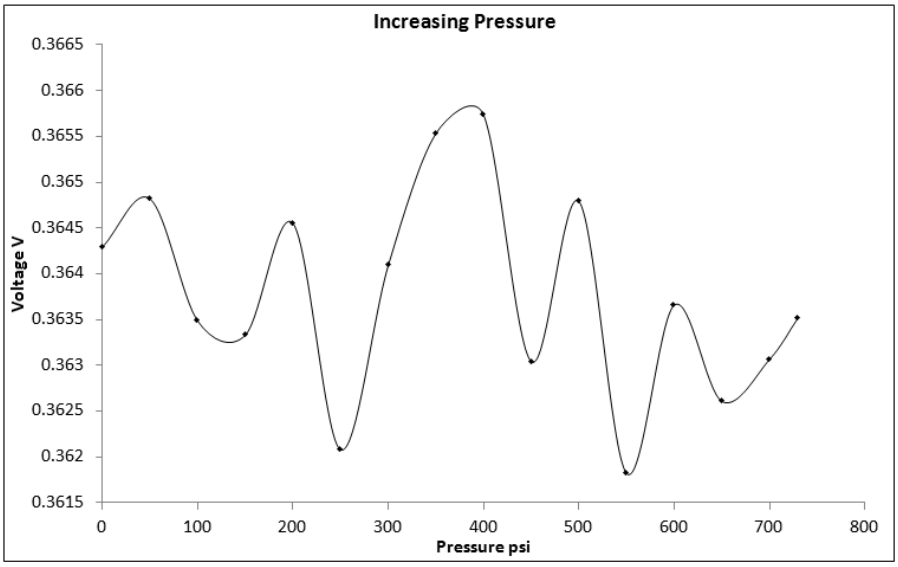

Figure 4.7. Aluminum diaphragm with increasing pressure one way.

The plots shown below in Figure 4.8(a), Figure 4.8(b) and Figure 4.8(c), illustrate the pressure cycling performed for the aluminum diaphragm. It was observed from the same that the diaphragm behaves erratically and results are not consistent. It was thus assumed that the gluing of the diaphragm to the tungsten carbide enclosures was not precise and it might have made the diaphragm rigid thereby restricting its deflections.

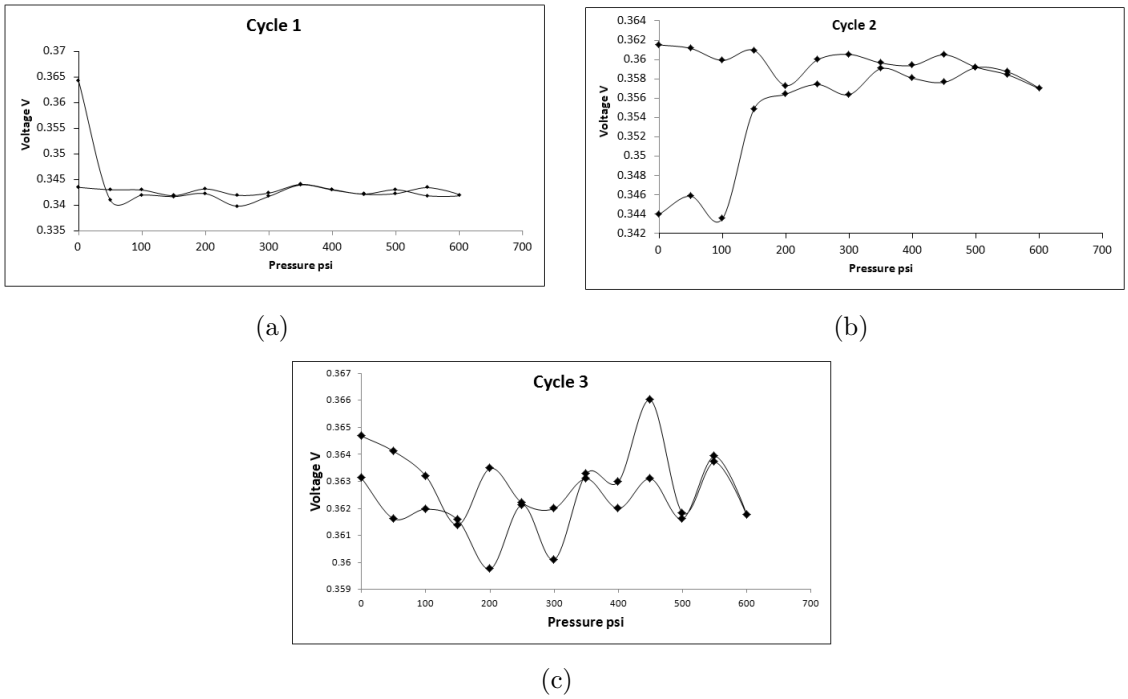

Figure 4.8. Aluminum diaphragm pressure cycling (a) Cycle 1 (b) Cycle 2 (c) Cycle 3.

A MEMS based diaphragm made of Nickel with a thickness of 20 mum was intended to be used. Due to time constraints and unavailability of the required equipment in the NANOFAB facility at The University of Texas at Arlington, the same could unfortunately not be manufactured.

CHAPTER 5

CONCLUSION AND RECOMMENDATIONS

5.1 Conclusion

A sensor was developed to determine the pressures and time-of-flight in a shock tube. High temperature materials and a transparent diaphragm were chosen so that the sensor can be further used for temperature measurements. The sensor was initially modelled with a transparent cubic zirconia as the diaphragm material. But cubic zirconia was not used due to the limitations of machining. Fused silica and aluminum were next tried as diaphragms. From the results, it was clear that the diaphragmswere deflecting with respect to pressure, but placement of the diaphragm required more accuracy and precision than was available. The diaphragm was manually glued on to the tungsten carbide enclosures whereas more sophisticated equipment is required. A micro-robotic hand connected to a computer to view a magnified image of the micro sensor can be used to apply the appropriate amount of glue and to place the diaphragm. The sensors were not tested in the shock tube because they have to be calibrated before being tested in the shock tube. The sensors were only tested in the calibration setup. The results shows that there were definite changes in the voltages when load was applied on the diaphragm; however, they were not consistent and repeatable.

5.2 Recommendations

5.2.1 Diaphragm thickness

From the calculations, it was assumed that the fused silica thickness should be $\approx$ 150 μm to withstand high pressures in harsh environments. It can be observed from the results that the deflections were very minimal due to the rigidity of the diaphragm. In order to obtain the expected results, diaphragm thickness should be between 50 μm and 75 μm depending upon the material used.

5.2.2 Higher pressure

The pressure used for calculation is 2000 psi and the diaphragm was designed accordingly with respect to the maximum load that can be applied arising from the expected pressures that can develop in detonation and shock tubes. But the maximum pressure that was available in the pressure bottle was 700psi. Moreover, due to lack of time and funding, many sensors were not able to be designed. Thus, there were limitations on the testing to the available pressure range to avoid damage to the sensor.

5.2.3 Placement of diaphragm

The diaphragm can be placed using micro robotic hands on top of the tungsten carbide enclosure. This may avoid the rigidity along the circumference since the placement will be precise on the step provided on the enclosure. The diaphragm can also be redesigned with a larger diameter (1.3 mm instead of 1 mm) which can be placed on top of the enclosure instead of placing it on the step. Glue used to attach the diaphragm to the enclosure plays a major role because it may cause rigidity which restricts the deflection. So the glue has to be applied carefully using the micro robotic

hands such that it doesn't overflow along the corners.

5.2.4 Fiber protection

The bare fibers used in the steel tubes are very fragile and tend to break often while working. So extra care has to be taken to protect them in order to avoid re working on the bare fibers polishing and assembling.

APPENDIX A

PCB PRESSURE TRANSDUCER CHARACTERISTICS

Table A.1. The performance properties for the pressure transducer (PCB Model 111A24)

Performance	English	SI
Measurement Range(for ± 5 V output)	1 kpsi	6895 kPa
Useful Overrange (for ± 10 V output)	2 kpsi	13790 kPa
Sensitivity(± 0.5 mV/psi)	5.0 mV/psi	0.73 mV/kPa
Maximum Pressure (static)	10 kpsi	68950 kPa
Resolution	0.020 psi	0.14 kPa
Resonant Frequency	$\geq$ 400 kHz	
Rise Time(Reflected)	$\leq$1:5 μs	
Low Frequency Response (-5%)	0.005 Hz	
Non-Linearity	$\leq$2.0%FS	

Table A.2. The environmental properties for the pressure transducer (PCB Model 111A24)

Environmental	English	SI
Acceleration Sensitivity	$<$ 0.002 psi/g	$<$0.0014 $kPa/(m/s^2)$
Temperature Range (Operating)	-100 to $+275°$ F	-73 to $+135°$C
Temperature Coeffcient of Sensitivity	$\leq$ 0.2%/°F	$\leq$ 0.36 %/°C
Maximum Flash Temperature	3000 °F	1649 °C
Maximum Vibration	2000 gpk	19614 m/s^2pk
Maximum Shock	20,000 gpk	196140 m/s^2pk

All these properties were provided on PCB's website for pressure transducer Model 111A24.

Table A.3. The electrical properties for the pressure transducer (PCB Model 111A24)

Electrical	
Output Polarity (positive pressure)	Positive
Discharge Time Constant (at room temp.)	$\geq$100 s
Excitation Voltage	20 to 30 VDC
Constant Current Excitation	2 to 20 mA
Output Impedance	$\leq$ 100 Ω
Output Bias Voltage	8 to 14 VDC

Table A.4. The physical properties for the pressure transducer (PCB Model 111A24)

Physical	English	SI
Sensing Geometry	Compression	
Sensing Element	Quartz	
Housing Material	17$-$4 Stainless Steel	
Diaphragm	Invar	
Sealing	Epoxy	
Electrical Connector	10$-$32 Coaxial Jack	
Weight	0.21 oz	6 gm

APPENDIX B

LASER SOURCE AND PHOTODETECTOR

B.1 DFB Laser Source

All these properties were provided on Thorlab's website for S3FC1550 - DFB fiber coupled laser source 1550nm.

B.1.1 Description

The Thorlabs Fiber Coupled Laser Sources provide easy coupling and simple control of laser diode driven fiber optics. These laser sources are available in two versions, Fabry-Perot and Distributed Feed Back (DFB). The Fabry-Perot version comes in five available wavelength choices from 635 nm to 1550 nm with standard single mode fiber or polarization maintaining fiber output. The DFB version comes equipped with a thermo-electric cooler to stabilize the output wavelength, and a 40 dB optical isolator to eliminate frequency jitter due to back-reflections. The DFB is available in 1310 nm and 1550 nm wavelengths.

B.2 Photodetector

All these properties were provided on Thorlab's website for DET01CFC - Fiber Input InGaAs Photodetector.

B.2.1 Description

The DET01CFC is a ready-to-use, high-speed InGaAs photodetector for use with FC/PC connectorized fiber optic cables in NIR optical systems. The unit comes with an FC/PC bulkhead connector, detector, and 12V bias battery enclosed in a compact aluminum housing. The FC/PC connector provides easy coupling to fiber-based light sources. The output uses an SMA jack to minimize size and maximize frequency response. The bandwidth is $2GHz$ and will operate over the spectral range

Table B.1. Specifications

Detector	$InGaAsPIN$
Active Diameter	$\varnothing 0.1mm$
Wavelength Range (λ)	800-1700nm
Peak Wavelength(λ_p)	1550 $nm(typ)$
Peak Response [$typ, \Re(\lambda_p)$]	0.95A/W (typ)
Input	FC/PC fiber connector
Rise/Fall Time (t_R)	$100ps(max)$
Ball Lens Size	$\varnothing 0.058''$ ($\varnothing$1.47 mm)
Reflective Index of lens	1.482 @ 675nm
Coupling Efficiency[4]	92% (typ)
Field of View	48°
Diode Capacitance (C_j)	1.0pF (1.2pF max)
Min Load Resistance	50Ω
Damage Threshold	70mW
Output Voltage[1] (Hi-Z)	0-10V
Output Voltage[2] (50Ω)	0-3.3V
Output	SMA (DC coupled)
Dark Current[3] (I_D)	0.7nA (2.5nA max)
Shunt Resistance (R_{sh})	1000MΩ
Weight	0.18lbs
Storage Temp	0-40 °
Operating Temp	0-40 °
Battery	$A23$, 12V_{DC}, 40mAh
NEP (1550nm)	1.5×10^{-15}W/$\sqrt{Hz}$ (max)
Bias Voltage (V_R)	12 V

of 800-1700nm. A visible version, the DET02AFC, is also available and operates in the 400-1100nm spectral range.

All measurements performed with a 50Ω load unless stated otherwise.

1. Into high impedance. Max voltage is dependent on battery voltage. New batteries typically show 12-13V, while drained batteries show 9V or less.
2. Calculated range based on peak responsivity and damage threshold.
3. Measured with specified bias voltage.

4. 92% into both single and multi-mode fibers over the full spectral response of detector.

REFERENCES

[1] Model 111a24 spec sheet. [Online]. Available: http://www.pcb.com

[2] Model 064b02 spec sheet. [Online]. Available: http://www.pcb.com

[3] F. R. Schauer, C. L. Miser, K. C. Tucker, R. P. Bradley, and J. L. Hoke, "Detonation initiation of hydrocarbon-air mixtures in a pulsed detonation engine," *43rd AIAA Aerospace Sciences Meeting*, pp. 1–10, January 2005.

[4] F. K. Lu, A. A. Ortiz, J. M. Li, C. H. Kim, and K. M. Chung, "Detection of shock and detonation wave propagation by cross correlation," *Mechanical Systems and Signal Processing*, vol. 23, no. 4, pp. 1098–111, 2009.

[5] ——, "Determining shock and detonation wave propagation time using wavelet methods," *39th AIAA Fluid Dynamics Conference*, pp. 1–15, 2009.

[6] W. N. MacPherson, J. M. Kilpatrick, J. S. Barton, and J. D. Jones, "Miniature fiber optic pressure sensor for turbomachinery applications," *American Institute of Physics*, vol. 70, pp. 1868–1874, 1999.

[7] W. N. MacPherson, M. J. Gander, J. S. Barton, J. D. Jones, C. L. Owen, A. J. Watson, and R. M. Allen, "Blast-pressure measurements with a high-bandwidth fibre optic pressure sensor," *Measurement Science and Technology*, vol. 11, pp. 95–102, 2000.

[8] R. A. Pinnock, "Optically pressure and temperature sensors for aerospace applications," *Sensor Review*, vol. 18, pp. 32–38, 1998.

[9] J. Zhou, S. Dasgupta, H. Kobayashi, H. E. Jackson, and J. T. Boyd, "Optically interrogated mems pressure sensors for propulsion applications," *Society of Photo-Optical Instrumentation Engineers*, vol. 40-4, pp. 598–604, April 2001.

[10] W. Pulliam and P. Russler, "High-temperature, high bandwidth, fiber-optic, mems pressure sensor technology for turbine engine component testing," *47th IIS*, pp. 1–10, 2001.

[11] S. Watson, W. N. MacPherson, J. S. Barton, J. D. C. Jones, A. Tyas, A. V. Pichugin, A. Hindle, W. Parkes, C. Dunare, and T. Stevenson, "Investigation of shock waves in explosive blasts using fibre optic pressure sensors," *Measurement Science and Technology*, vol. 17, pp. 1337–1342, 2006.

[12] Thorlabs.com - det10c high-speed ingaas detector, 700-1800 nm, 10 ns rise time.

[13] K. Betzler, "Fabry-perot interferometer," *Universit at Osnabruck*, 2002.

[14] J. M. Kilpatrick, W. N. MacPherson, J. S. Barton, J. D. C. Jones, D. R. Buttsworth, T. V. Jones, K. S. Chana, and S. J. Anderson, "Measurement of unsteady gas temperature with optical fibre fabry-perot microsensors," *Measurement Science and Technology*, vol. 13, pp. 706–712, 2002.

[15] Y. Kim and D. P. Neikirk, "Micromachined fabry-perot cavity pressure transducer," *IEEE Photonics Technology Letters*, vol. 7-12.

[16] A. Mendez, T. F. Morse, and K. A. Ramsey, "Mcromachined fabry-perot interferometer with corrugated silicon diaphragm for fiber optic sensing applications," *Integrated Optics and Microstructures*, vol. 1793, pp. 170–182, 1992.

[17] X. Wang, B. Li, O. L. Russo, H. T. Roman, K. K. Chin, and K. R. Farmer, "Diaphragm design guidelines and an optical pressure sensor based on mems technique," *Microelectronics Journal*, vol. 37, pp. 50–56, 2005.

[18] M. Li, M. Wang, and H. Li, "Optical mems pressure sensor based on fabry-perot interferometry," *Optics express*, vol. 14, pp. 1497–1504, 20 February 2006.

[19] D. C. Abeysinghe, S. Dasgupta, J. T. Boyd, and H. E. Jackson, "A novel mems pressure sensor fabricated on an optical fiber," *IEEE photonics technology letters*, vol. 13, pp. 993–995, September 2001.

[20] A. A. Ortiz, "Development of spectral and wavelet time-of-flight methods for propagating shock and detonation waves," Master's thesis, The University of Texas at Arlington, December 2008.

[21] Wire edm, sinker edm, edm hole driling services, applegate edm. [Online]. Available: http://www.applegateedm.com

[22] Material: Tungsten carbide (wc), bulk. [Online]. Available: https://www.memsnet.org

[23] Aremco: High temperature adhesives, ceramics, potting compounds, sealants, screen printers, dicing saws, furnaces. [Online]. Available: http://www.aremco.com

[24] Oequest - components - passive components - polarization maintaining (pm) couplers/splitters - pm fused couplers - 1x2 1550nm pm fused fiber coupler. [Online]. Available: http://www.oequest.com

[25] Fiber optic patch cables. [Online]. Available: http://www.cablesondemand.com

[26] W. P. Eaton, F. Bitsie, J. H. Smith, and D. W. Plummer, "A new analytical solution for diaphragm deflection and its application to a surface-micromachined pressure sensor," *Modeling and Simulation of Microsystems*, 1999.

[27] Optical windows. [Online]. Available: http://www.tempotec.com

[28] Thorlabs.com - g14250 5-minute epoxy, general purpose - two part. [Online]. Available: http://www.thorlabs.com

[29] Tungsten carbide information - provided by insaco inc, 215-536-3500. [Online]. Available: http://www.insaco.com

[30] Thorlabs.com - fiber polishing supplies. [Online]. Available: http://www.thorlabs.com

[31] E. J. Ruggiero, "Modeling and control of spider satellite components," Ph.D. dissertation, Virginia Tech, year =.

[32] E. Ventsel and T. Krauthammer, *Thin plates and shells: theory, analysis, and applications*. Marcel Dekker Inc., July 2001.

[33] S. Timoshenko and S. Woinosky-Kreiger, *Theory of plates and shells*. McGraw Hill Classic, 1987.

[34] http://home.davidson.com.au/products/strain/mg/technology/technotes/tn510.pdf. [Online]. Available: www.measurementsgroup.com

[35] efunda: Plate calculator – clamped circular plate with uniformly distributed loading. [Online]. Available: http://www.efunda.com

[36] W. Parkes, V. Djakov, J. S. Barton, S. W. W. N. MacPherson, J. T. M. Stevenson, and C. C. Dunare, "Design and fabrication of dielectric diaphragm pressure sensors for applications to shock wave measurement in air," *Journal of Micromechanics and Microengineering*, vol. 17, pp. 1334–1342, 2007.

[37] *Evaluation of glued-diaphragm fibre optic pressure sensors in a shock tube*, vol. 16, 2007.

[38] J. Xu, X. Wang, K. L.Cooper, and A. Wang, "Miniature all-silica fiber optic pressure and acoustic sensors," *Optics Letters*, vol. 30, 2005.

[39] Materials properties. [Online]. Available: http://accuratus.com

[40] Cubic zirconia information - provided by insaco inc, 215-536-3500. [Online]. Available: http://www.insaco.com

[41] R. S. Figliola and D. E. Beasley, *Theory and design for mechanical measurements*. Hoboken, N.J.: John Wiley, 2006. [Online]. Available: 4.1.1 Publisher description http://www.loc.gov

[42] Periodic table of elements: Aluminum - al (environmentalchemistry.com). [Online]. Available: http://environmentalchemistry.com

[43] Ni labview - the software that powers virtual instrumentation - national instruments. [Online]. Available: http://www.ni.com

BIOGRAPHICAL STATEMENT

Karthikeyan Jagadevan was born in Chennai, Tamil Nadu, India in 28^{th} September 1983.

He joined Bachelor of Engineering in Instrumentation and Control Engineering in 2001 at SRM Engineering College affiliated to Anna University and fulfilled his wish of learning an advanced technology. He received his B.E. degree fromAnna University, Chennai, India, in 2005. He then worked as a software engineer with Accenture services, Chennai, India. The desire for his passion with aerospace made him pursue Master of Science degree Aerospace Engineering with The University of Texas at Arlington.